JOURNAL OF COMPUTATIONAL PHYSICS 97, 1–29 (1991)

A Numerical Scheme for the Solution of the Space Charge Problem on a Multiply Connected Region

C. J. BUDD AND A. A. WHEELER

School of Mathematics, University Walk, Bristol BS8 1TW, United Kingdom

Received November 28, 1988; revised June 5, 1990

In this paper we extend the work of Budd and Wheeler (*Proc. R. Soc. London A* **417**, 389, 1988), who described a new numerical scheme for the solution of the space charge equation on a simple connected domain, to multiply connected regions. The space charge equation, $\nabla \cdot (\Delta\bar{\varphi}\, \nabla\bar{\varphi}) = 0$, is a third-order nonlinear partial differential equation for the electric potential $\bar{\varphi}$, which models the electric field in the vicinity of a coronating conductor. Budd and Wheeler described a new way of analysing this equation by constructing an orthogonal coordinate system $(\bar{\varphi}, \bar{\psi})$ and recasting the equation in terms of x, y, and $\Delta\bar{\varphi}$ as functions of $(\bar{\varphi}, \bar{\psi})$. This transformation is singular on multiply connected regions and in this paper we show how this may be overcome to provide an efficient numerical scheme for the solution of the space charge equation. This scheme also provides a new method for the solution of Laplaces equation and the calculation of orthogonal meshes on multiply connected regions.

INTRODUCTION

In this paper we extend a new numerical scheme [6] for the solution of the space charge equation, $\nabla \cdot (\Delta\bar{\varphi}\, \nabla\bar{\varphi}) = 0$, for the electric potential $\bar{\phi}$, in two spatial dimensions which arises in the study of steady electric fields in the neighbourhood of a coronating conductor, to multiply connected regions. In contrast to an electrostatic field where the charge density is everywhere zero, the fields in this situation have a nonzero charge density which is known as the space charge. Such ionised fields arise when there is a high DC electric field due to a conductor maintained at a high electric potential. This field causes a local breakdown of the air molecules into positive and negative ions and a glowing corona forms around the conductor. The ions which have the opposite sign to that of the conductor are attracted onto its surface whereas those of the same sign leave the neighbourhood of the corona and enter the medium surrounding the conductor creating a space charge. Experiments

0021-9991/91 $3.00

indicate that the region occupied by the corona is very thin and thus a macroscopic description of our system consists of studying the field derived from a single ion species with the thin corona acting as a source of these ions. This, so-called space charged situation has been the subject of a number of papers. Early references include Townsend [29], Felici [14], Atten [4], and Khalifa [19] with more recent work by Janischewskyj and Gela [17], Morrow [21], Sigmond [24], Abdel-Salam *et al.* [1, 2], Okubo *et al.* [22], Sunaga and Sawada [27], Smith [26], Budd [7], Hutton [15], and Varley [31].

The partial differential equation that describes this field may be expressed as an elliptic and a hyperbolic equation coupled together in a nonlinear manner. It is the mixed type of the space charge equation that provides the main difficulty in the construction of an efficient numerical algorithm. This is because such an algorithm must cope with both the features of hyperbolic systems, such as shock formation and propagation of initial data, as well as the global and smoothing properties of elliptic systems. Thus in much of the earlier numerical work many approximations were made concerning the distribution of the characteristics in order to simplify the problem. One in particular, known as Deutch's approximation (see [23]), assumes the field lines to be the same as the field lines obtained by finding a harmonic field with zero space charge. It will be evident from the calculations presented here that this approximation is grossly in error for the field lines in a multiply connected region. In contrast, more recent work on the numerical solution of the space charge equations has employed finite element techniques. Although this can be very successful (see [2, 15]), it is also expensive, requiring a special treatment at the shock boundaries and a careful mesh refinement close to the high tension conductor. The method described by Budd and Wheeler [6] is designed to exploit the mixed type of the space charge equation by treating the elliptic and hyperbolic parts separately using appropriate numerical techniques within an iterative framework. This is done by identifying the characteristics of the system as the electric field lines which are used to construct an orthogonal coordinate system where one of the coordinates describes the characteristics. Thus the hyperbolic part of the system is integrated directly along the characteristics and the elliptic part is solved using a finite difference scheme. The method has the further advantage that the orthogonal coordinate system is body fitted and so deals with arbitrarily shaped domains by transforming them to the unit square. However, this transformation does depend crucially on the connectedness of the domain and in this paper we demonstrate how the singularity in this transformation which occurs when the domain is multiply connected may be dealt with.

The fields arising from an ionised gas are important in the study of DC transmission lines, cyclone separators, electrostatic scrubbers, granular bed filters, and electrostatic precipitators used in electricity power stations for the removal of dust from furnace gases. A summary of other industrial applications of electrostatic phenomena is given by Cross [11]. In many cases realistic geometries are multiply connected, for example, an electrostatic precipitator comprises, in general, of an array of thin coronating electrodes at high potential between two parallel earthed

plates. This geometry is illustrated in Fig. 1 and it is evident from this figure that it is multiply connected. It has been shown recently [5] that on such multiply connected regions the solution to the space charge equation may have solutions in which the gradient of the space charge density is discontinuous; this has been observed experimentally in a test rig at the Central Electricity Generating Board, CERL, Leatherhead.

In Section 2 we describe a simple model of an ionised gas and derive the space charge equation. Further, we pose two problems which relate to simple models of an electrostatic precipitator and an experimental rig at the National Bureau of Standards, Maryland, USA [20] which provide different multiply connected geometries on which to test our numerical scheme. In Section 3 we introduce the hodograph transformation used by Budd and Wheeler [6] for simply connected domains and describe in detail the algorithm based on this transformation for the multiply connected domains considered here. In Section 4 we exploit the fact that the solution of the space charge equation is harmonic when the space charge density is everywhere zero. Thus we compare results from our numerical scheme in this special case to harmonic solutions generated from an algorithm that employs the Schwarz–Christoffel conformal map and also with a boundary integral method. In Section 5 we present results of our method for the two model problems posed in Section 2. Finally, in Section 6 we give our conclusions.

2. The Governing Equation

We consider the electric field in the vicinity of a coronating conductor. In this situation the corona formed on the conductor, due to the electrical breakdown of air in the presence of the locally high electric field, provides a source of electric charge. This charge migrates under the influence of the electric field to give rise to a nonzero space charge density in the neighbourhood of the conductor. In this situation the current $\mathbf{j}$ is described by

$$\mathbf{j} = \mu\bar{\rho}\mathbf{E}, \tag{2.1}$$

where $\bar{\rho}$ is the space charge density, $\mathbf{E}$ is the electric field and μ is the mobility of the charge, which is assumed constant and for typical applications $\mu \sim 2 \times 10^{-4} m^2 V^{-1} s^{-1}$. We consider the steady situation, in which case from Maxwell's equations $\nabla \wedge \mathbf{E} = 0$ and we therefore deduce the existence of an electric potential $\bar{\varphi}$. In terms of this potential $\mathbf{E} = -\nabla\bar{\varphi}$ and $\bar{\rho} = -\varepsilon_0 \Delta\bar{\varphi}$, where ε_0 is the permittivity of air. Finally, conservation of electric charge gives

$$\nabla \cdot \mathbf{j} = 0. \tag{2.2}$$

Combining Eqs. (2.1) and (2.2) we obtain

$$\nabla \cdot (\Delta\bar{\varphi}\, \nabla\bar{\varphi}) = 0, \tag{2.3}$$

which we shall refer to as the space charge equation. This is a third-order nonlinear partial differential equation for $\bar{\varphi}$ which we consider here in two spatial dimensions. The characteristic determinant associated with it has two imaginary roots $dy/dx = \pm i$ as well as a real root $dy/dx = \bar{\varphi}_x/\bar{\varphi}_y$. Hence there is a one-parameter family of real characteristic curves which are orthogonal to the equipotentials and so represent the electric field lines. The space charge equation may be written as

$$\varepsilon_0 \frac{d\bar{\rho}^{-1}}{ds} = -|\nabla\bar{\varphi}|^{-1}, \qquad \text{on} \quad \frac{dy}{dx} = \frac{\bar{\varphi}_x}{\bar{\varphi}_y}, \tag{2.4a}$$

$$\bar{\rho} = -\varepsilon_0 \Delta\bar{\varphi}, \tag{2.4b}$$

where s is the arclength along a field line measured such that s increases with $\bar{\varphi}$. Thus we may decompose (2.3) into an elliptic Poisson equation coupled to the characteristic ordinary differential equation in a nonlinear manner. We note that the special case $\bar{\rho} = 0$ is a solution of (2.4a), in which case φ is a harmonic function. The numerical solution of (2.3) on simply and one-connected domains, using a hodograph method, has been considered previously by Budd and Wheeler [6]. Here we extend the hodograph method to multiply connected domains; specifically we consider a domain of the form illustrated in Fig. 1. However, we consider two sets of boundary conditions associated with this domain which gives rise to two different problems for $\bar{\varphi}$, which we refer to as Problems I and II.

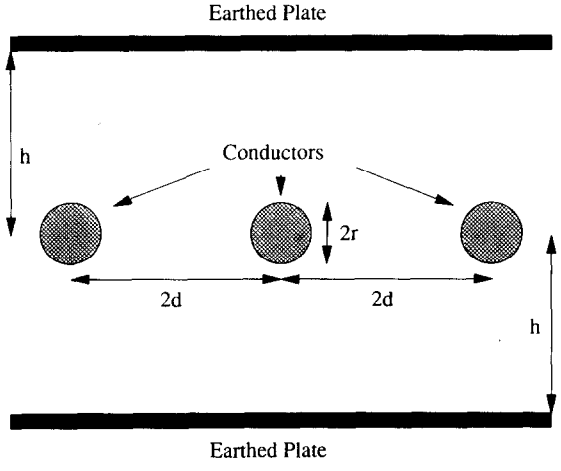

FIG. 1. A schematic diagram of an electrostatic precipitator.

Problem I. We consider a periodic array of conductors all at the same potential situated midway between two parallel plates at a lower potential. The conductors have alternately zero and nonzero space charge specified on their surfaces. From a consideration of the symmetry and periodicity present in this problem we pose the following equivalent problem for the electric potential on the subdomain $\tilde{\Omega}$

$$\left.\begin{aligned} \frac{d\rho^{-1}}{ds} &= |\nabla\varphi|^{-1}, \\ \rho &= \Delta\varphi, \end{aligned}\right\} \quad \mathbf{x} \in \tilde{\Omega},$$

$$\begin{aligned} \rho &= 0, \quad \varphi = 0, \quad \mathbf{x} \in \partial\Omega_1, \\ \rho &= \rho_0 \quad (>0), \quad \varphi = 0, \quad \mathbf{x} \in \partial\Omega_3, \\ \varphi_x &= 0, \quad x \in \partial\Omega_4 \cup \partial\Omega_6, \\ \varphi_y &= 0, \quad x \in \partial\Omega_2 \cup \partial\Omega_5, \\ \varphi &= 1, \quad x \in \partial\Omega_5, \end{aligned} \tag{2.5}$$

where we have nondimensionalised $\bar{\varphi}$ with respect to the potential difference between the conductors and the parallel plates, Φ, by defining $\varphi = 1 - \bar{\varphi}/\Phi$, and the distance with respect to half of the distance between the centres of the conductors, d. Hence the space charge is nondimensionalised by defining $\bar{\rho} = \varepsilon_0 \Phi \rho / d^2$ and so $\rho_0 = \bar{\rho}_0 d^2/\varepsilon_0 \Phi$ is the nondimensional surface charge on $\partial\Omega_3$ and $\bar{\rho}_0$ is the corresponding dimensional quantity. We have chosen these scalings as it proves convenient in our numerical scheme to arrange for φ to increase, away from the conductor on which the space charge is prescribed. The problem is shown diagrammatically in Fig. 2(i) in which $\partial\Omega_i$, $i = 1, 6$ are defined. The constants α and β are the nondimensional conductor radius r/d and the aspect ratio h/d, respectively.

The motivation for the study of this problem derives from a simple model of the electric field in electrostatic precipitators used to remove fly ash from coal fired electric power station flue gases. In these devices an array of high potential coronating wires are situated between parallel earthed plates through which the flue gases are passed. This results in the precipitation of fly ash on the plates and hence the cleansing of the flue gas. The geometry shown in Fig. 1 corresponds to that of an experimental test precipitator at CERL, Leatherhead, England. Experimental results from this device are presented in Corbin [9].

Problem II. We consider a single cylindrical conductor placed between two parallel horizontal plates. The space charge density on the upper plate together with the electric potential is given. On the conductor the electric potential is prescribed to be equal to that of the upper surface and the space charge density is set to zero. The lower surface is grounded and so here we only prescribe the

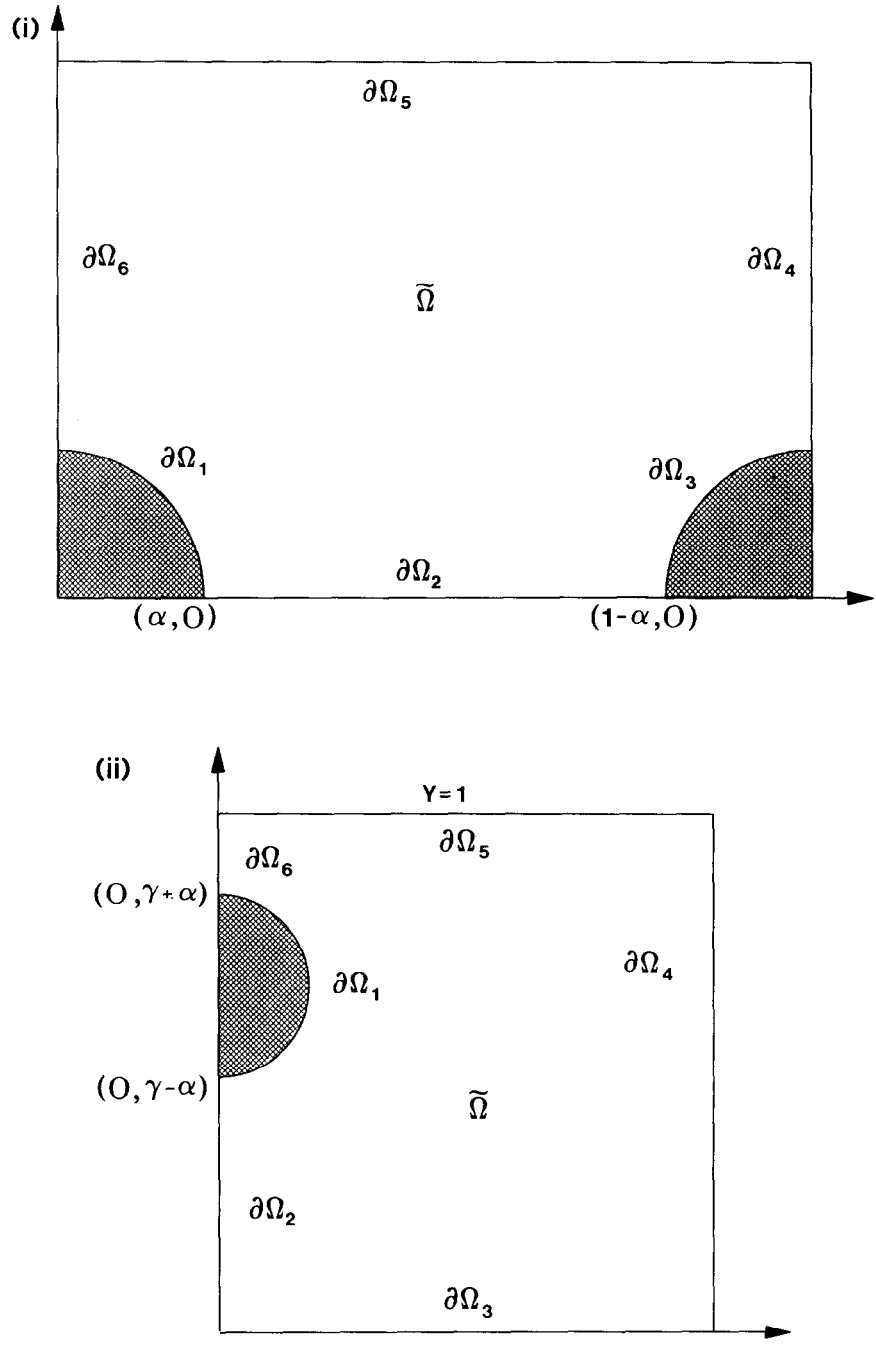

FIG. 2. (i) and (ii) The domain $\tilde{\Omega}$ for the Problems I and II, respectively.

electric potential to be zero. The mathematical statement for the non dimensional potential φ is

$$\left.\begin{aligned} \frac{d\rho^{-1}}{ds} &= |\nabla\varphi|^{-1}, \\ \rho &= \Delta\varphi, \end{aligned}\right\} \quad \mathbf{x} \in \tilde{\Omega},$$
$$\rho = 0, \qquad \varphi = 0, \qquad \mathbf{x} \in \partial\Omega_1,$$
$$\varphi_x = 0, \qquad \mathbf{x} \in \partial\Omega_2 \cup \partial\Omega_4 \cup \partial\Omega_6 \tag{2.6}$$
$$\rho = \rho_0\ (>0), \qquad \varphi = 0, \qquad \mathbf{x} \in \partial\Omega_3,$$
$$\varphi = 1, \qquad \mathbf{x} \in \partial\Omega_5,$$

where we have employed the same nondimensionalisation as before. The problem is illustrated in Fig. 2(ii) where the boundaries $\partial\Omega_i$, $i = 1, 6$, are also defined. This problem serves as a simple model of an experimental rig employed at the National Bureau of Standards, USA [20] to investigate the effect of electrical measuring devices on space charge electrostatic fields. It also is related to the electrode configuration in a thermionic tetrode.

In both of the above problems we have prescribed the space charge density on the high potential conductor. In many applications this conductor acts as a source of space charge through the mechanism of corona discharge. This is commonly modelled by prescribing the electric field intensity at this conductor surface to be constant at the smallest value required for corona onset, Kaptzow [18], which for dry air is approximately 3 MVm^{-1}. The numerical scheme that we describe in this paper can be simply modified to deal with this situation, as noted in Section 3.2.

3. The Numerical Method

Our numerical method is based upon a hodograph transformation of the space charge equation. Below we briefly describe the transformation. For a more detailed account the reader is referred to Budd and Wheeler [6].

3.1. *The Hodograph Transformation*

Part of the difficulty in obtaining an accurate numerical solution to the space charge equation lies in the fact that the characteristic equation is to be integrated along characteristic curves which are themselves part of the solution. This is related to the underlying mixed type of the space charge equations indicating that the solution has properties associated with both elliptic and hyperbolic partial differential equations. The elliptic part is a statement that a particle of charge instantaneously sets up an electric field everywhere in the medium, whereas the hyperbolic part arises from the finite velocity at which charged particles move under the influence

of the electric field. To overcome this difficulty we define a new variable ψ such that the level curves of ψ are everywhere orthogonal to the level curves of φ. Thus we define ψ by

$$\nabla\varphi \cdot \nabla\psi = 0, \tag{3.1}$$

and so ψ acts as a label for the characteristics. The identity (3.1) is in general satisfied if

$$\begin{aligned} \varphi_x &= \lambda\psi_y, \\ \varphi_y &= -\lambda\psi_x, \end{aligned} \tag{3.2}$$

where λ is a function which at this stage is undetemined. We now exploit this description of the characteristic curves and recast the space charge equation (2.3) along with (3.2) in terms of φ and ψ as independent variables, with x, y, λ, and ρ as the dependent variables. It can be shown, Budd and Wheeler [6], that this procedure gives

$$\begin{aligned} \lambda &= a(\psi)/\rho, \qquad \rho \neq 0, \\ \lambda &= a(\psi), \qquad \rho = 0, \end{aligned} \tag{3.3}$$

where $a(\psi)$ is function of a single variable and the space charge equation (2.4) becomes

$$\begin{aligned} y_\psi &= a(\psi)\,\sigma x_\phi, \\ x_\psi &= -a(\psi)\,\sigma y_\phi, \end{aligned} \tag{3.4a}$$

$$\sigma_\phi = x_\phi^2 + y_\phi^2, \qquad \text{for} \quad \rho \in (0, \infty), \tag{3.4b}$$

where

$$\sigma = \begin{cases} 1/\rho, & \rho \neq 0, \\ 1, & \rho = 0, \end{cases}$$

along with the appropriate transformed boundary conditions. The function $a(\psi)$, and hence λ, are dependent upon the manner in which ψ is specified on the boundary of the domain. These functions may be regarded as Lagrange multiplier terms deriving from the orthogonality constraint (3.1) and they are also related to the current flowing in the gas. Indeed, if we consider two field lines labelled ψ_1 and ψ_2 then the current, I, flowing across any equipotential surface orthogonal to these lines is precisely

$$I = \int_{\psi_1}^{\psi_2} a(\psi)\, d\psi.$$

The above transformation is only valid provided it is invertible, i.e., the Jacobian, $|\partial(x, y)/\partial(\varphi, \psi)| \in (0, \infty)$. In general this is not true and it fails if the electric field strength $|\mathbf{E}| = (\varphi_x^2 + \varphi_y^2)^{1/2}$ becomes zero. However, it is known [5], that there exists a maximum principle for φ. This in conjunction with simple topological arguments based on Morse's theory can be used to establish that the above condition will be violated at only one point in the domain of problems I and II. At this point φ will have a saddle point and we denote the value of φ there by φ^*. (This saddle point is evident in the results of our calculations presented in Figs. 8, 9, 10). It is the presence of the saddle point that provides the additional complication that must be overcome to apply the hodograph method to multiply connected regions. In Fig. 3(i) we illustrate the images of Ω, $\partial\Omega_i$, $i = 1, 6$, denoted by Ω' and $\partial\Omega_i'$, respectively, under this transformation. The mathematical statement of each problem consists of the transformed governing equations (3.4) allied with the appropriate boundary conditions which are

Problem I.

$$\begin{gathered}
\rho = 0, \qquad x = \alpha \cos \frac{\pi}{2}\{1 - f(\psi)\}, \qquad y = \alpha \sin \frac{\pi}{2}\{1 - f(\psi)\}, \qquad (\varphi, \psi) \in \partial\Omega_1', \\
y = x_\psi = 0, \qquad (\varphi, \psi) \in \partial\Omega_2', \\
\rho = \rho_0, \qquad x - 2 = \alpha \cos \frac{\pi}{2}\left(2 - g\left(\psi - \frac{1}{2}\right)\right), \\
y = \alpha \sin \frac{\pi}{2}\left(2 - g\left(\psi - \frac{1}{2}\right)\right), \qquad (\varphi, \psi) \in \partial\Omega_3', \qquad (3.5) \\
x = 2, \qquad y_\psi = 0, \qquad (\varphi, \psi) \in \partial\Omega_4', \\
y = \beta, \qquad x_\phi = 0, \qquad (\varphi, \psi) \in \partial\Omega_5' \\
x = y_\psi = 0, \qquad (\varphi, \psi) \in \partial\Omega_6'.
\end{gathered}$$

Problem II.

$$\begin{gathered}
\rho = 0, \qquad x = \alpha \frac{\pi}{2}(1 - 2h(\psi)), \qquad y = \gamma + \alpha \sin \frac{\pi}{2}(1 - 2h(\psi)), \qquad (\varphi, \psi) \in \partial\Omega_1', \\
y_\psi = x = 0, \qquad (\varphi, \psi) \in \partial\Omega_2' \cup \partial\Omega_6', \\
x = k(\psi - \tfrac{1}{2}), \qquad y = 0, \qquad \rho = \rho_0, \qquad (\varphi, \psi) \in \partial\Omega_3', \qquad (3.6) \\
x = 1, \qquad y_\psi = 0, \qquad (\varphi, \psi) \in \partial\Omega_4', \\
y = 1, \qquad x_\phi = 0, \qquad (\varphi, \psi) \in \partial\Omega_5'.
\end{gathered}$$

Here f, g, h, k are suitable monotonic functions from $[0, \frac{1}{2}]$ to $[0, 1]$ that relate

ψ to the geometry of the domain in physical space by specifying ψ in terms of arc length along the conductors.

We note that in both cases the transformed domain Ω' in (φ, ψ)-space consists of the unit square penetrated by the branch cut Γ_1 defined by $\Gamma_1 = \{(\varphi, \psi); \varphi \in [0, \varphi^*], \psi = \frac{1}{2}\}$, where φ^* must be determined as part of the solution.

The advantages of this transformation are

(i) it maps curvilinear domains in physical space to the same unit square in (φ, ψ)-space albeit with a branch cut.

(ii) The characteristic curves in physical space are transformed to known fixed straight lines $\psi = \text{const}$, allowing the characteristic equations to be dealt with more easily.

(iii) The functions f, g, h, and k are not unique for a given problem and so may be used to distribute the ψ coordinates in physical space as desired. In particular, we can effectively refine the grid by a suitable choice of these functions.

(iv) The technique determines φ and ψ and hence generates an orthogonal grid defined by (φ, ψ) coordinates in the physical domain. Thus this method provides a new and efficient way of generating orthogonal meshes and is related to the work of Thompson *et al.* [28] and Arina [3].

In both Problems I and II ρ is prescribed to be a zero only on $\partial\Omega_1'$. From the characteristic equation (2.4a) we therefore deduce that $\rho \equiv 0$ in the subdomain $\Omega_1' = [0, 1] \times [0, \frac{1}{2})$ and so φ is harmonic on Ω_1'; hence $\sigma \equiv 1$ on Ω_1'. The constraint that $\rho_0 > 0$ and hence that σ is positive on $\partial\Omega_3'$, along with the characteristic equation (2.4a), implies that σ is strictly positive on $\Omega_2' = [0, 1) \times (\frac{1}{2}, 1]$. These considerations indicate that the solution on the curve $\Gamma_2' = \{(\varphi, \psi): \varphi^* < \varphi < 1, \psi = \frac{1}{2}\}$ will be nonsmooth. From the analysis given in Budd, Friedman, McLeod, and Wheeler [5] it is shown that ρ has a discontinuous derivative across the curve Γ_2'. Hence there is a weak shock on Γ_2'. To deal with this situation we require appropriate shock conditions for x and y on Γ_2'. These are obtained by insisting that x, y, x_ϕ, and y_ϕ are continuous across Γ_2', from which we deduce from (3.4b) that

$$x(\varphi, \psi)\big|_{\psi = 1/2^-}^{\psi = 1/2^+} = y(\varphi, \psi)\big|_{\psi = 1/2^-}^{\psi = 1/2^+} = 0 \tag{3.6}$$

and

$$\frac{x_\psi}{\lambda(\varphi, \psi)}\bigg|_{\psi = 1/2^-}^{\psi = 1/2^+} = \frac{y_\psi}{\lambda(\varphi, \psi)}\bigg|_{\psi = 1/2^-}^{\psi = 1/2^+} = 0, \tag{3.7}$$

for $\varphi \in [\varphi^*, 1]$. These conditions augment the boundary conditions (3.5) and (3.6) of Problems I and II, respectively.

We now consider the numerical solution of Problems I and II using a finite difference method.

3.2. *The Finite Difference Scheme*

The expression of the space charge equations in the transformed space given in (3.4) naturally leads to an algorithm that treats the hyperbolic characteristic equations (3.4b) and elliptic system (3.4a) separately. The we have adopted the following two-stage algorithm employing a fixed point iteration

1. Guess x, y, a, φ^*.
2. Stage I. Update σ by numerically integrating (3.4b) in the region $[0, 1] \times [\frac{1}{2}, 1]$.
3. Stage II. Update x, y, a, φ^* (and hence λ) by numerically solving the system (3.4a).
4. Test for convergence. If converged; stop; otherwise; repeat steps 2 to 4.

One of the purposes of the hodograph transformation is to deal with the characteristic curves by mapping them to the fixed straight lines ψ constant in Ω'. Thus the numerical integration of the characteristic equation in stage I is straightforward. Another funtion of the transformation is to map the physical domain to a rectangular domain. This simplifies the numerical solution of the elliptic system (3.4a) and allows us to implement a finite difference scheme in stage II. However, the branch cut present in Ω' along with the determination of $a(\psi)$ and φ^* presents a major difficulty.

As φ^* is part of the solution, the extent of the branch cut is undetermined and so presents a complication in defining a finite difference mesh. We overcome this by adopting the linear transformation

$$\tilde{\varphi} = \begin{cases} \dfrac{\varphi}{2\varphi^*}, & 0 \leqslant \varphi \leqslant \varphi^* \\ \dfrac{2\varphi^* - 1 - \varphi}{2(\varphi^* - 1)}, & \varphi^* < \varphi \leqslant 1 \end{cases} \tag{3.9}$$

which maps the branch point to $\tilde{\varphi} = \frac{1}{2}$. For simplicity of notation we henceforth omit the tilde, in which case the governing equations (3.4) become

$$\begin{aligned} y_\psi &= \gamma(\varphi)\, \sigma a(\psi) x_\phi, \\ x_\psi &= -\gamma(\varphi)\, \sigma a(\psi)\, y_\phi, \end{aligned} \tag{3.10a}$$

and

$$\sigma_\phi = \gamma(\varphi)(x_\phi^2 + y_\phi^2), \tag{3.10b}$$

where

$$\gamma(\varphi)=\begin{cases}\dfrac{1}{2\varphi^*}, & 0\leqslant\varphi<\dfrac{1}{2}\\[2ex] 1, & \varphi=\dfrac{1}{2}\\[2ex] \dfrac{1}{2(1-\varphi^*)}, & \dfrac{1}{2}\leqslant\varphi\leqslant 1.\end{cases}$$

This transformed domain is shown in Fig. 3(ii).

We now consider our finite difference mesh. It proves necessary to employ two different uniform meshes, both having grid spacings $\delta\varphi$ and $\delta\psi$ in the φ and ψ directions, respectively. On one, which we refer to as grid α we define the nodes at which we approximate x and y. On the other, which we refer to as mesh β, we approximate σ and $a(\psi)$. The variables $X^n_{i,j}$, $Y^n_{i,j}$, A^n_j, and $\Sigma^n_{i,j}$ denote the finite difference approximations to the nth iterates of x, y, a, and σ, respectively, at the node (i, y) of the appropriate mesh. The two meshes are centrally offset from one another as shown in the finite difference molecule in Fig. 4.

The branch cut Γ_1', along with the two shock conditions on Γ_2', necessitates that we devote two consecutive rows of mesh α to represent the solution on $\Gamma_1'\cup\Gamma_2'$. The two meshes are shown in Fig. 5, also serves to define the various parameters N_{mid}, N_ϕ, N_{bc}, N_{bc1}, and N_ψ associated with both meshes. The nodes in the adjacent rows defined by $j=N_{bc}$ and $j=N_{bc1}$ of mesh α approximate x, y, and a on either side of $\Gamma_1'\cup\Gamma_2'$. On the rows defined by $1\leqslant i\leqslant N_{bc}$ of mesh β, $\Sigma^n_{i,N_{bc}}$ is undefined due to the presence of the branch cut. The fact that $\rho\equiv 0$ on Ω_1' implies from (3.3) that $\sigma\equiv 1$ there and, so, we set $\Sigma^n_{i,j}=1$ for $1\leqslant i\leqslant N_\phi$, $1\leqslant j\leqslant N_{bc}$, $n\geqslant 0$.

We now describe stages I and II in detail:

Stage I. This stage updates σ in Ω_2' from the current iterates of x, y, a, and φ^* by integrating the characteristic equation (3.10b), using the initial data on σ given at $\varphi=0$. Because we are constrained to working on a fixed mesh we employ the trapezium rule at interior points of Ω_2', which is $O(h^2)$ accurate, allied with a backward difference at the initial step. Thus

$$\frac{(\Sigma^n_{i,j}-\sigma_0)}{\delta\varphi}=\gamma_i\left\{\left[\frac{D(X^n_{i,j})}{2\delta\varphi}\right]^2+\left[\frac{D(Y^n_{i,j})}{2\delta\varphi}\right]^2\right\},\qquad i=1$$

and

$$\frac{(\Sigma^n_{i+1,j}-\Sigma^n_{i,j})}{\delta\varphi}=\gamma_i\left\{\left[\frac{D(X^n_{i,j})\,\gamma_i+D(X^n_{i+1,j})}{4\delta\varphi}\right]^2+\left[\frac{D(Y^n_{i,j})+D(Y^n_{i+1,j})}{4\delta\varphi}\right]^2\right\},\qquad(3.11)$$

for $i=2$, $N_\phi-1$, and $N_{bc1}\leqslant j<N_\psi-1$, where D is the difference operator defined by $D(S^n_{i,j})=\{S^n_{i+1,j}+S^n_{i+1,j+1}-(S^n_{i,j}+S^n_{i,j+1})\}$, and $\gamma_n=\gamma((n-1)\,\delta\varphi)$.

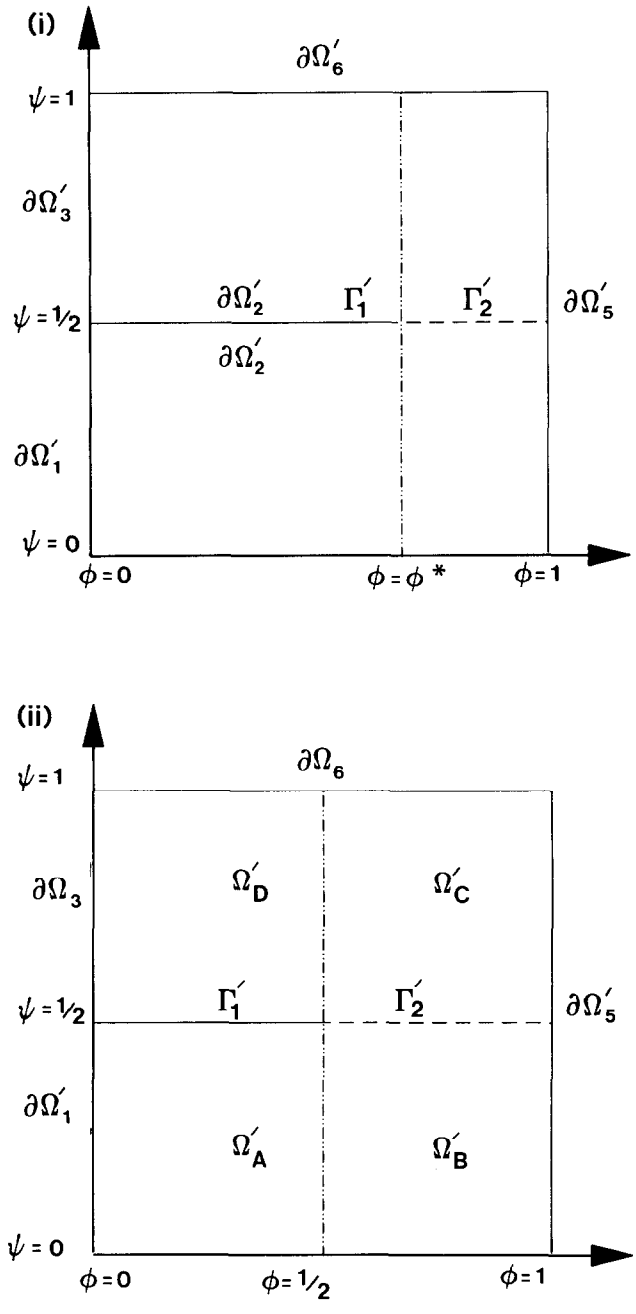

FIG. 3. (i) The transformed domain. (ii) The transformed domain after application of the second transformation (3.9).

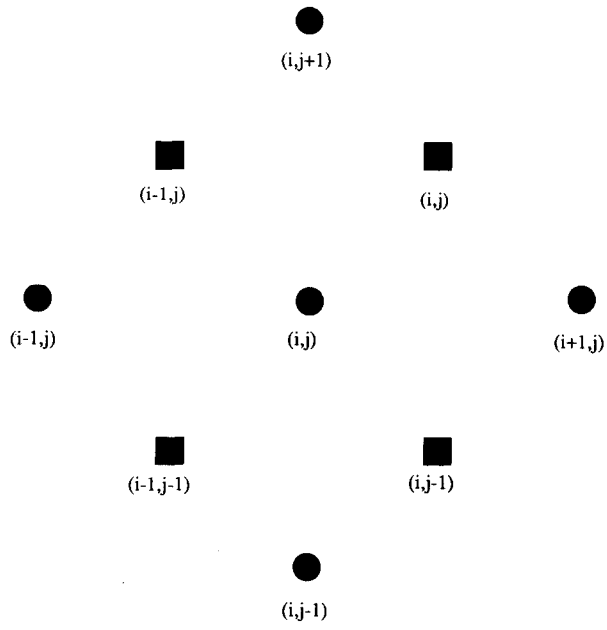

FIG. 4. A finite difference molecule indicating the relation between meshes α and β indicated by ■ and ●, respectively.

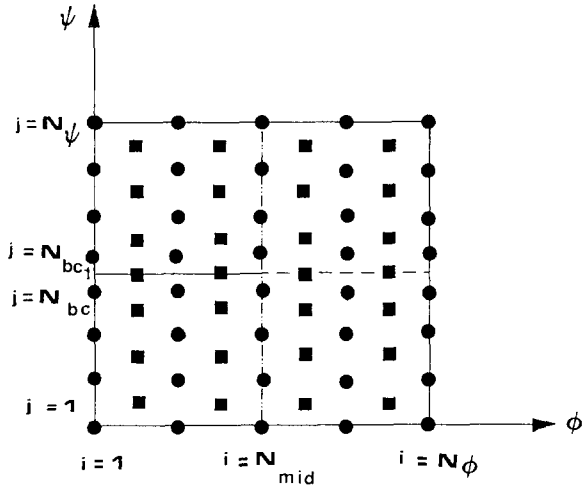

FIG. 5. The relationship of the finite difference meshes to the transformed domain. Here meshes α and β are indicated by ■ and ●, respectively.

Stage II. At this stage we update the estimates of x, y, a, and φ^*. We proceed in two steps. In the first, which we refer to as II(i) we solve elliptic problems for x and y and in the second we update a and φ^*.

Step II(i). The elliptic system (3.10a) can be combined to give

$$\begin{aligned}(\lambda x_\phi \gamma(\varphi))_\phi + \left(\frac{x_\psi}{\lambda\gamma(\varphi)}\right)_\psi &= 0,\\ (\lambda y_\phi \gamma(\varphi))_\phi + \left(\frac{y_\psi}{\lambda\gamma(\varphi)}\right)_\psi &= 0.\end{aligned} \tag{3.12}$$

We apply a second-order finite difference formulation of (3.12) using mesh α and based on the molecule shown in Fig. 4. Thus

$$\begin{aligned}&\frac{\gamma_{i+1/2}(Z^k_{i+1,j}-Z^k_{i,j})\,\bar{A}^n_{i,j}-\gamma_{i-1/2}(Z^k_{i,j}-Z^k_{i-1,j})\,\bar{A}^n_{i-1,j}}{\delta\varphi^2}\\ &\quad+\frac{(Z^k_{i,j+1}-Z^k_{i,j})/(\gamma_i\tilde{A}^n_{i,j})-(Z^k_{i,j}-Z^k_{i,j-1})/(\gamma_i\tilde{A}^n_{i,j-1})}{\delta\psi^2}=0,\end{aligned} \tag{3.13}$$

where $k=1,2$. We define $Z^k_{i,j}$ by $Z^i_{i,j}=X^n_{i,j}$, $Z^2_{i,j}=Y^n_{i,j}$, $\bar{A}_{i,j}=(\Sigma^n_{i,j}A^n_{i,j}+\Sigma^n_{i,j-1}A^n_{i,j-1})/2$, and $\tilde{A}_{i,j}=(\Sigma^n_{i,j}A^n_{i,j}+\Sigma^n_{i-1,j}A^n_{i-1,j})/2$. The boundary conditions on x and y are simple Dirichlet or Neuman conditions; we apply them by employing a standard second-order finite difference formulation [25] at the external boundaries, $\partial\Omega_i$, $i=1,6$. On the branch cut boundary $\partial\Omega_2'$ we have similar boundary conditions which are discretised in the same way on the two rows $j=N_{bc}$ and $j=N_{bc1}$ for $1\leqslant i<N_{br}$. On the remaining nodes of these two rows the branch point is treated and the shock conditions (3.6), (3.7) are employed. At the two nodes $i=N_{br}$, $j=N_{bc}, N_{bc1}$, which *both* correspond to the branch point, we apply the conditions that $y=0$ and $x_{\phi\phi}=0$ at the node $i=N_{br}$, $j=N_{bc}$ and continuity of x and y at the other in a straightforward manner. At the remaining nodes on the row $j=N_{bc}$ we similarly employ continuity of x and y. For those of row $j=N_{bc1}$ we invoke the shock conditions (3.7). As x_ψ and y_ψ are discontinuous across Γ_2' we use second-order, one-sided differences to approximate these ψ derivatives on either side of Γ_2. This leads to the discretisation

$$\begin{aligned}&\frac{Z^k_{i,(N_{bc}-2)}}{\tilde{A}^n_{i,(N_{bc}-2)}}-\left(\frac{3}{\tilde{A}^n_{i,(N_{bc}-1)}}+\frac{1}{\tilde{A}^n_{i,(N_{bc}-2)}}\right)Z^k_{i,N_{bc}-1}\\ &\quad+\left(\frac{3}{\tilde{A}^n_{i,(N_{bc}-1)}}+\frac{3}{\tilde{A}^n_{i,(N_{bc1})}}\right)Z^k_{i,N_{bc}}\\ &\quad-\left(\frac{3}{\tilde{A}^n_{i,N_{bc1}}}+\frac{1}{\tilde{A}^n_{i,(N_{bc1}+1)}}\right)Z^k_{i,N_{bc1}}\\ &\quad+\frac{Z^k_{i,(N_{bc1}+2)}}{\tilde{A}^n_{i,(N_{bc1}+2)}}=0,\end{aligned} \tag{3.14}$$

for $N_{bc}<i<N\varphi$.

The above finite difference scheme yields a system of linear equations for both x and y of the form

$$\mathbf{A}^k\mathbf{Z}^k = \mathbf{b}, \qquad k = 1, 2, \tag{3.15}$$

where $\mathbf{Z}^k = (Z^k_{1,1}, Z^k_{1,2}, ..., Z^k_{N_\phi N_\psi})^T$, and $\mathbf{A}^k$ are sparse square matrices or order $N_\phi \times N_\psi$. The presence of the branch cut Γ_1' and the shock boundary Γ_2 ensures the $\mathbf{A}^1$ and $\mathbf{A}^2$ have a nonstandard structure and so Stone's Implicit Procedure [16] which was employed for solving the space charge equations on simply connected domains, Budd and Wheeler [6], cannot be used here. Instead, we have numerically solved (3.15) by a direct method; in particular, we used NAG routines F01BRF and F01BSF which enables us to exploit the fact that the sparsity pattern is the same at each iteration. This leads to a considerable increase in the speed of execution of the algorithm. We now go on to consider the updating procedure for a and φ^* in step II(ii).

Step II(ii). The current iterates of x and y obtained in the previous step approximate the solution of the elliptic systems (3.12) and therefore do not, in general, satisfy the original orthogonality conditions (3.1a) from which they are derived. At this step we employ (3.10a) to update $a(\psi)$ and φ^*. The presence of the branch cut again presents a difficulty because of the singularity associated with it. It may be shown [5] that ρ vanishes at the branch point and hence near this point $\varphi(x, y)$ satisfies an approximation to Laplace's equation. A simple calculation then shows that $\varphi(x', y') \approx x'^2 - y'^2$ and $\psi(x', y') \approx 2x'y' \log x'$, where x', y' are the x and y coordinate distances from the saddle point in the region in which the space charge is nonzero. We invert these two expressions to determine the local behaviour of x' and y' in terms of φ and ψ to obtain the expressions

$$\begin{aligned} x_\phi &\sim \frac{x'}{2s'^2}, & y_\phi &\sim -\frac{y'}{2s'^2}, \\ x_\psi &\sim y' \frac{\log x'}{2s'^2}, & y_\psi &\sim x' \frac{\log x'}{s'^2}, \end{aligned} \tag{3.16}$$

and

$$\sigma \sim \log x', \qquad \text{as} \quad x', y', s' \to 0,$$

where $s' = \sqrt{x'^2 + y'^2}$, thus x_ψ and y_ψ are singular at the branch point. Hence any estimate of $a(\psi)$ made directly from Eqs. (3.10a) will be ill-conditioned near the branch point. However, we overcome this by estimating $a(\psi)$ in two ways, both integrals of (3.10a). These are

$$\begin{aligned} &\frac{1}{\gamma(\varphi)} \int_0^1 w(\varphi, \psi)\, \rho y_\psi \, d\varphi \Big/ \int_0^1 w(\varphi, \psi)\, x_\phi \, d\varphi, \\ &-\frac{1}{\gamma(\varphi)} \int_0^1 w(\varphi, \psi)\, \rho x_\psi \, d\varphi \Big/ \int_0^1 w(\varphi, \psi)\, y_\phi \, d\varphi, \end{aligned} \tag{3.17}$$

where $w(\varphi, \psi)$ is a suitable weighting function such that $w(\varphi, \psi) \sim (\varphi - \frac{1}{2})^2$, $\varphi \to \frac{1}{2}$.

We use an integral formulation to reduce the errors associated with the numerical differentiation involved in approximating x_ψ and x_ϕ. Further, we choose to evaluate ρx_ψ, as the above local analysis at the branch point indicates that this is less singular than x_ψ alone. The weighting function is introduced to further reduce numerical errors associated with the singularity in the gradient of ρx_ψ. In our numerical scheme we evaluate the integrals using the trapezium rule. The associated numerical error is proportional to $(w\rho x_\psi)_{\phi\phi}$ and so the error with the above choice of weighting function is proportional to $(\varphi - \frac{1}{2})^{-1/2}$ close to the branch point. Using

error but this has not been found to be the case in our calculations due to the coarseness of the mesh close to the branch point.

In order to update $a(\psi)$ we construct three different estimates of $a(\psi)$, denoted by $a^i(\psi)$, $i = 1, 3$, from

$$a^i(\psi) = [\mu a_{\text{old}} + |I_i|]/[\mu + |J_i|] \tag{3.18}$$

where $I_i = \int_{L_i}^{U_i} w(\varphi, \psi)\, \rho f_i\, d\varphi / \int_{L_i}^{U_i} w(\varphi, \psi)\, d\varphi$, $J_i = \int_{L_i}^{U_i} w(\varphi, \psi)\, \rho g_i\, d\varphi / \int_{L_i}^{U_i} w(\varphi, \psi)\, d\varphi$, $i = 1, 3$, where $L_1 = L_2 = 0$, $L_3 = U_1 = U_2 = \frac{1}{2}$, $U_3 = 1$, $f_1 \equiv f_3 \equiv x_\psi$, $f_2 \equiv y_\psi$, $g_1 \equiv g_3 \equiv y_\psi$, $g_2 \equiv x_\phi$, and $\mu \in [0, 1]$ is a relaxation parameter, typically taken to be 0.25. Thus $a^1(\psi)$ and $a^2(\psi)$ are estimates of $a(\psi)$ derived from the region $0 \leqslant \varphi < \frac{1}{2}$ and $a^3(\psi)$ from $\frac{1}{2} \leqslant \varphi \leqslant 1$. A further consideration of the boundary conditions on $\partial\Omega_4'$, $\partial\Omega_6'$, and Γ_1' for Problem I indicates that a^1 is good estimate of $a(\psi)$ away from the branch cut and a^2 is a good estimate near the branch cut. For Problem II, similar remarks apply. However, for clarity we limit our detailed discussion below of this stage of the algorithm to Problem I. Thus to obtain a single estimate of $a(\psi)$ from the region $0 \leqslant \varphi \leqslant \frac{1}{2}$ we take a weighted combination as follows: We define $\zeta = 2\,|\psi - \frac{1}{2}|$ and $\omega(\zeta) = \zeta^4[3 - \zeta^2]$; then we take

$$\hat{a}(\psi) = \omega(\zeta)\, a^1(\psi) + [1 - \omega(\zeta)]\, a^2(\psi)$$

as our new estimate of $a(\psi)$. In constructing the above estimates for $a(\psi)$, namely $\hat{a}(\varphi)$ and $a^3(\varphi)$, we determine A_j^n (which is defined on mesh β) by using standard second-order finite differences, using the adjacent nodes on mesh α, to determine the various derivatives of x and y required in the integrals I_i and J_i, $i = 1, 3$. It remains to construct the new estimate for φ^* and a single new estimate for $a(\psi)$. We update φ^* by insisting the two estimates $\hat{a}$ and a^3 are continuous at the branch point as φ increases through $\frac{1}{2}$. To do this we recognise that both $\hat{a}$ and a^3 are linearly dependent on φ^* through $\gamma(\varphi)$. It is easily shown that this continuity requirement yields

$$\frac{\varphi'}{\varphi^*}\,\hat{a}\bigg|_{\varphi = \varphi^*} = \left(\frac{1 - \varphi'}{1 - \varphi^*}\right) a^3\bigg|_{\varphi = \varphi^*},$$

where φ' is a new estimate for φ^*. In practice the branch point is represented as a node in mesh α and so we use quadratic extrapolation to estimate a_3 and $\hat{a}$ at the

branch point from both the regions $\psi < \frac{1}{2}$ and $\psi > \frac{1}{2}$, which in turn yields two estimates for φ' which we denote φ'_- and φ'_+, respectively. We calculate a new single estimate from

$$\varphi' = \mu\varphi^* + \frac{(1-\mu)}{2}(\varphi'_- + \varphi'_+)$$

and finally we update $a(\psi)$ from

$$a(\psi) = \frac{1}{2}\left[\frac{\varphi'}{\varphi^*}\hat{a}(\psi) + \left(\frac{1-\varphi'}{1-\varphi^*}\right)a^3(\psi)\right]$$

and hence $A^n_{i,j}$ from the identity $\lambda = a(\psi)\sigma$.

As in Section 2, for practical applications it is preferable to prescribe the electric field at the conductor surface at a critical value E^*, rather than the space charge density. To achieve this we modify Stage I of the algorithm described here by making use of the identity

$$\frac{ds}{d\psi} = a\sigma/E^*,$$

where s is the arclength along the conductor surface, which is derived in Budd and Wheeler [6]. This allows, at Stage I, a new value of σ to be estimated along the conductor surface by

$$\Sigma^n_{0,j} = E^* \left.\frac{ds}{d\psi}\right|^{n-1}_j \Big/ A^{n-1}_{0,j},$$

which replaces the initial value of σ (which was previously prescribed) for the characteristic equation (3.4b).

4. A Test Problem

As noted earlier the solution of the space charge equation is harmonic when ρ_0, the space charge density on the conductors is zero. Thus in this special case the method described above provides a new technique for solving Laplace's equation on a multiply connected domain. The only modification required is to omit stage I of the algorithm so that $\sigma \equiv 1$ and hence $\rho = 0$ everywhere on the domain. In this section we exploit this special case to provide a test on our algorithm. In particular, we consider a modified version of Problem I in which $\rho_0 = 0$ and the conductors $\partial\Omega_1$ and $\partial\Omega_3$ are replaced by squares of side length $2d$. Thus we have to solve Laplace's equation on a polygonal T-shaped domain and so we employed the Schwarz–Christoffel conformal transformation

$$w(z) = f_1(z) = \frac{(d+1)}{2}(1+i) + C\int_0^z \prod_{k=1}^{k=6}(z - z'/z_k)^{-\beta_k}\,dz',$$

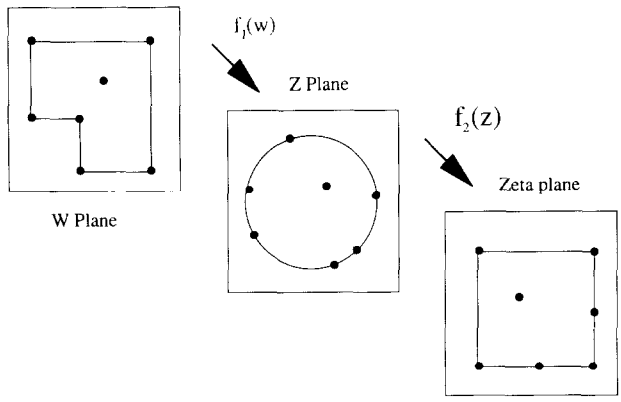

FIG. 6. The Schwarz–Christoffel transformations and associated complex planes employed in the test problem described in Section 4.

which maps the unit disk in the complex z-plane to half of the T-shaped domain in the complex w-plane as shown in Fig. 6. The constants β_k, $k = 1, 6$, are the exterior angles of the polygon in the w-plane. The remaining constant C and prevertices z_k, $k = 1, 6$, were determined numerically using the algorithm SCPACK due to Trefethen [30]. A further Schwarz–Christoffel map $f_2(z)$ was employed to map the unit disk to a rectangle in the ζ-plane as shown in Fig. 6. In this way the solution was determined, the value of φ^* being given by $\mathrm{Im}(w_5)$ and the electric field by $f_2'(z')/f_1'(z')$. The results from SCPACK were double-checked against the NAG algorithm D03EAF which employs a boundary integral method and were found to be in satisfactory agreement. We found that the NAG algorithm employing 300 points on the boundary took approximately the same amount of CPU time as our method. In Table I we compare the values of φ^* obtained by our method using a

TABLE I

	φ^*	
I	Hodograph method (22 × 44 grid)	SCPACK
0.03125	0.703716	0.763216
0.0625	0.672522	0.709043
0.125	0.607674	0.622887
0.25	0.464637	0.467639
0.3	0.404260	0.405955
0.4	0.282137	0.283525
0.5	0.167246	0.169667
0.6	0.076649	0.077716
0.7	0.030590	0.021015

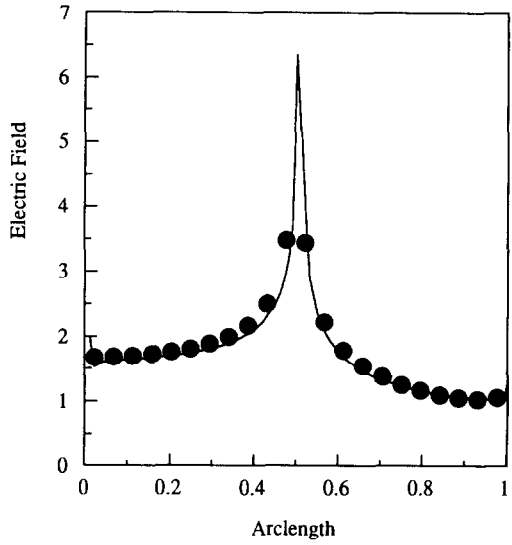

FIG. 7. A comparison of the calculated values of the electric field on the square conductor of side 0.6 between the Schwarz–Christoffel technique employing SCPACK [30] denoted by the solid curves and our method indicated by ●. Here s is the arclength along the conductor measured in an clockwise sense from the point (0, 0.3) divided by 0.6.

22×44 grid to those obtained by SCPACK for different values of d. In general the agreement is good, although for small values of d the disparity increases. However, we consider this test problem to be a severe test of our algorithm due to the singularity in the electric field present at the corner of the square conductors; the severity of which increases as the size of the squares decreases. This factor in itself may account for the worse agreement with SCPACK at smaller values of d. In Fig. 7 we compare the electric field at the edge of the square conductor obtained by our method and SCPACK. These are in satisfactory agreement showing a maximum error on the vertical side of the conductor; $\{x = 0.3,\ 0 \leqslant y \leqslant 0.3\}$. We attribute this to the proximity of the saddle point which is closest to this side. Overall, however, the error is the order of 1–2%. The values of the electric field obtained by the NAG boundary integral method were in better agreement with SCPACK except near (0, 0.3) and (0.3, 0), where it was in error by approximately 30%.

5. RESULTS

In this section we present results from our numerical calculations for both Problems I and II. All the calculations were performed using a 22×44 grid with the functions f, g, h, k defined to be $f(\psi) \equiv g(\psi) \equiv h(\psi) \equiv k(\psi) \equiv 2\psi$ and took at the most 20 cpu min on a VAX 11/780 to converge to within an error of less than 10^{-6}

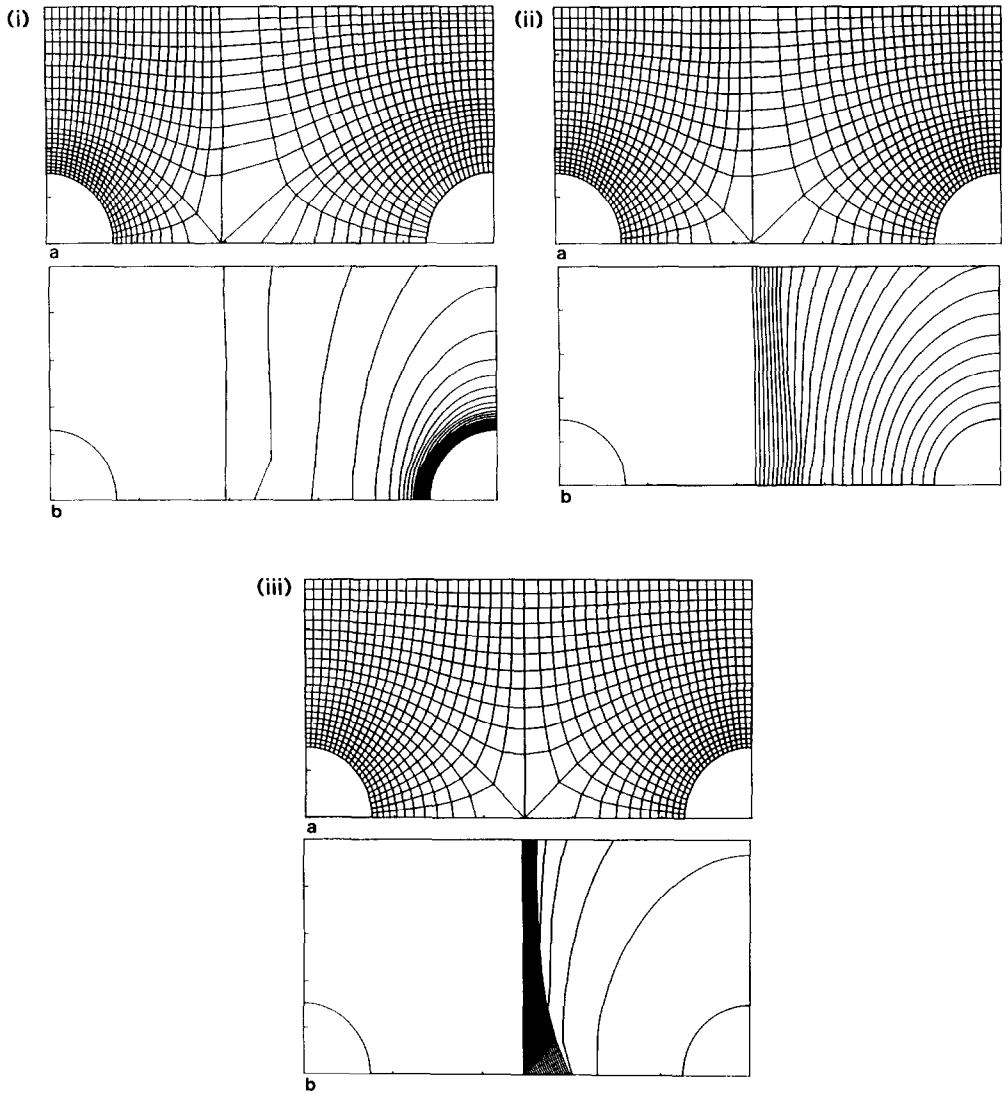

FIG. 8. (i)(a) The field lines and equipotentials for Problem I and (b) the corresponding 24 equally spaced contours of space charge density for the case $\rho = 10$. (ii)(a) The field lines and equipotentials for Problem I and (b) the corresponding 24 equally spaced contours of space charge density for the case $\rho = 1$. (iii)(a) The field lines and equipotentials for Problem I and (b) the corresponding 24 equally spaced contours of space charge density for the case $\rho = 0.1$.

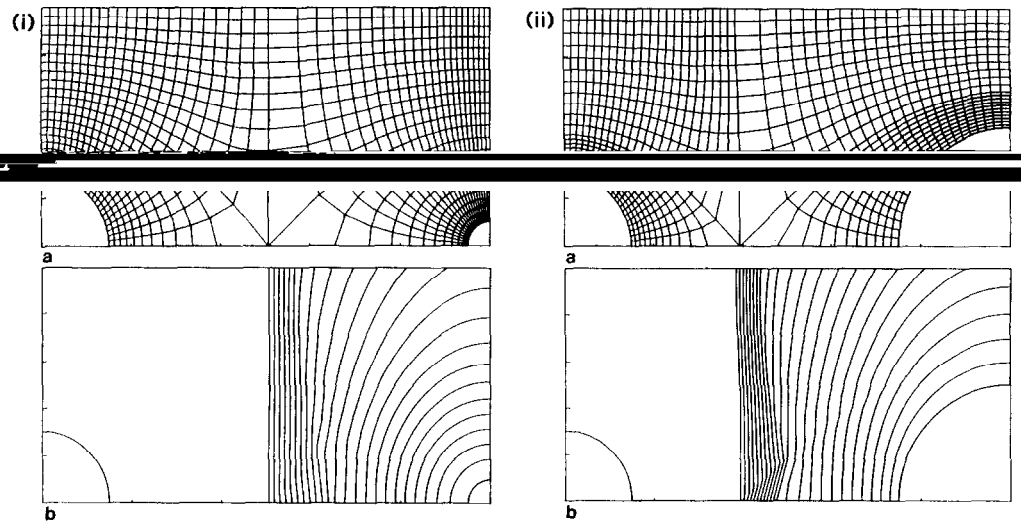

FIG. 9. (i)(a) The field lines and equipotentials for Problem I and (b) the corresponding 24 equally spaced contours of space charge density for the case $\rho = 1$, $\alpha = 0.1$. (ii)(a) The field lines and equipotentials for Problem I and (b) the corresponding 24 equally spaced contours of space charge density for the case $\rho = 1$, $\alpha = 0.5$.

in the successive iterates of $a(\psi)$. The results are displayed in Fig. 8, 9, and 10, and the associated values of φ^* are given in Table II.

For Problem I calculations were performed for a variety of values of ρ_0 and α with $\beta = 1.0$. The results are displayed in Figs. 8, 9, and 10. We see from Fig. 8 that the effect of increasing the space charge on the right-hand cylinder is to cause the space charged region to increase in size with the saddle point moving away from the charged conductor. With a space charge density of 10 on the right-hand conductor the saddle point moved to approximately $x = 0.8$. We found that as the space charge on the right-hand conductor increased the saddle point moved monotonically towards the uncharged conductor and its position tended to approximately 0.8. We attribute this change in position of the saddle point to the

FIG. 10. (i)(a) The field lines and equipotentials calculated for Problem II and (b) the corresponding 25 equally spaced contours of space charge density for the case $\rho_0 = 10$, $\alpha = 0.05$, $\gamma = 00.7$. (ii)(a) The field lines and equipotentials calculated for Problem II and (b) the corresponding 25 equally spaced contours of space charge density for the case $\rho_0 = 1$, $\alpha = 0.05$, $\gamma = 0.7$. (iii)(a) The field lines and equipotentials calculated for Problem II and (b) the corresponding 25 equally spaced contours of space charge density for the case $\rho_0 = 0.1$, $\alpha = 0.05$, $\gamma = 0.7$. (iv) The field lines and equipotentials calculated for Problem II for the case $\rho_0 = 0$, $\alpha = 0.05$, $\gamma = 0.7$. (v)(a) The field lines and equipotentials calculated for Problem II and (b) the corresponding 25 equally spaced contours of space charge density for the case $\rho_0 = 10$, $\alpha = 0.1$, $\gamma = 0.6$. (vi)(a) The field lines and equipotentials calculated for Problem II and (b) the corresponding 25 equally spaced contrours of space charge density for the case $\rho_0 = 1$, $\alpha = 0.2$, $\gamma = 0.6$.

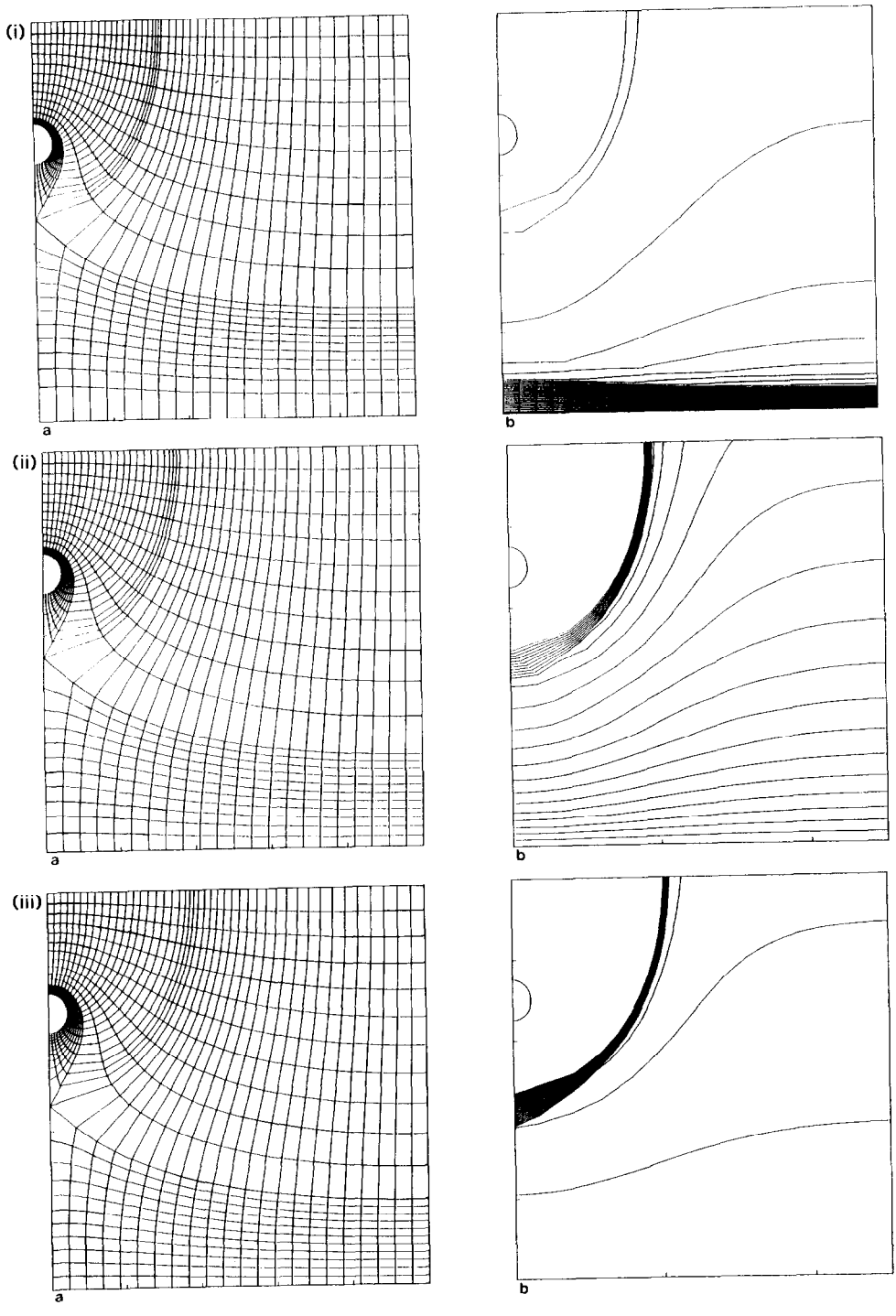
(i)
a
b
(ii)
a
b
(iii)
a
b

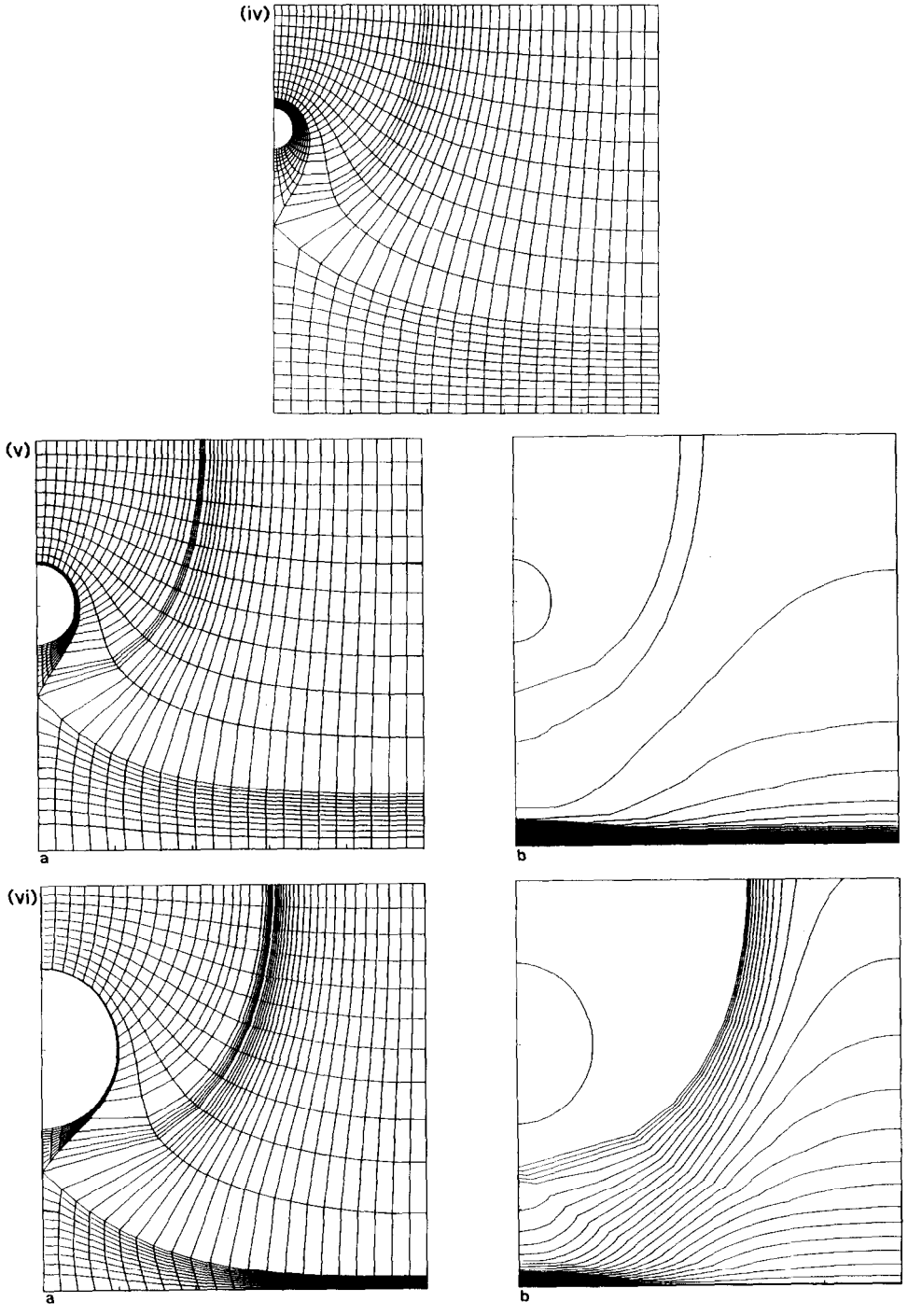

FIG. 10—*Continued*

TABLE II

Figure	φ^*
8.1	0.3447
8.2	0.4151
8.3	0.4739
9.1	0.5233
9.2	0.3203
10.1	0.1288
10.2	0.1488
10.3	0.1788
10.4	0.1854
10.5	0.0438
10.6	0.0146

mutual repulsion of the field lines due to the presence of the space charge. At the same time the value of φ^* decreased and tended to a limiting value of approximately 0.34. From Figs. 8 and 9 it is clear that the presence of the space charge decreases the electric field strength at the charged conductor and to a lesser extent increases the electric field on the earthed plate. In the latter case this increase is consistent with the decrease in the value of φ^* with increasing space charge on the conductor. These effects are most apparent in Fig. 8(i), where $\rho_0 = 10$ for which the field in the space charged region is less at the conductor than at the earthed plate. Further, in the space charge free region the electric field is greater at the conductor than the earthed plate.

In Figs. 8(ii), 9(i), and 9(ii) and Tables I and II we consider the effect of changing the radius of the charged conductor alone; the value of ρ_0 is unity in each case. In the absence of space charge the effect of reducing the size of the right-hand conductor is that it causes the saddle point in the electric potential to move towards it. However, it is clear from these figures that the inclusion of space charge opposes this effect. We have also carried out calculations relevant to the CERL experimental precipitator. This consists of an array of conductors of radius 3 mm at a potential of -45 kV between two grounded parallel plates separated by 300 mm. The value of ρ_0, the space charge density at the conductor surface, was taken to be 100 μCm^{-3}. Our calculations agreed very favourably with the experimental results, prediting the observed current to within 5%.

In Figs. 10 and Table II we display the results of our calculations for Problem II. In this case our method was less successful. The equipotentials and field lines lose orthogonality near the cylinder on the side adjacent to the saddle point. We tried various parameterisations of the conductor than the uniform one shown in Figs. 10, as well as other weighting functions w and ω but to no effect, the non-orthogonality persisted and the value of φ^* showed some dependence on these factors. It is clear that it is the presence of the saddle point that is the ultimate cause of the difficulty

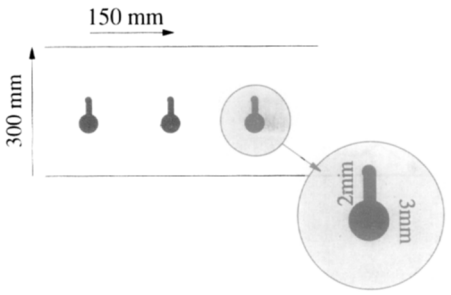

FIG. 11. The experimental rig of an electrostatic preciptator used in the experiments conducted by Corbin [9].

which is exacerbated by the very small values of φ^*, which results in a very non-uniform grid. This is borne out by observing that this nonorthogonality becomes more apparent as φ^* decreases. However, we believe the solutions are otherwise satisfactory. Similar effects are observed as in Problem I, resulting in a shadow in the space charge upon the grounded plate, due to the repulsion of charge away from the uncharged conductor. The extent of space charge shadow decreases as the space charge density on the charged plate increases. Further, a space charge boundary layer forms on the charged conductor as the space charge increases for both Problems I and II.

In Figs. 8, 9, and 10 for the space charge density a slight discontinuity in the gradient of the space charge is apparent near the saddle point. We attribute this

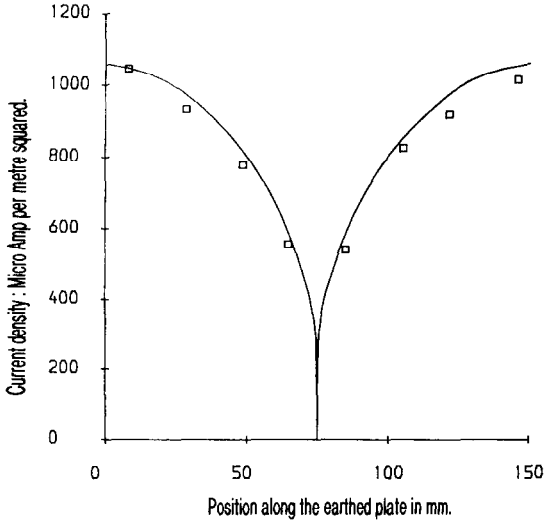

FIG. 12. The current density distribution along the earthed plate; □ represent experimental values and solid lines represent calculated values.

feature to the linear interpolation used by our contouring algorithm which produces significant errors when the points in the (x, y)-plane are sparsely distributed.

We have also conducted a series of numerical experiments using this algorithm for a realistic experimental electrostatic precipitator configuration used by the CEGB [9]. In this we consider a row of barbed electrodes 150 mm apart at a potential of 50 kV placed between two grounded plates separated by 300 mm. The situation is illustrated in Fig. 11. For this calculation we prescribe the electric field to be $3\ \mathrm{MVm}^{-1}$ and employ the modified algorithm described at the end of Section 3.2. In Fig. 12 we present a graph of both the calculated and experimental current distribution obtained by Corbin [9] along the grounded plates. These results are in very good agreement; in particular, the pronounced dip in the current density midway between the electrodes is well represented.

6. Conclusions

We have shown how the hodograph method develop by Budd and Wheeler [6] may be extended to multiply connected regions. This method has many advantages; primarily, that it is able to cope well with the mixed type of the space charge equations by separating the hyperbolic and elliptic components of the equation. Further, it does not rely on the specific shapes of the conductors and grounded surfaces for its implementation. It also provides as a spin-off a new method for calculating orthogonal grids on multiply connected and simply connected regions. It is particularly suitable for this purpose as it directly calculates the coordinate values of the nodes of such a mesh and, further, the mesh generated may be modified by altering the value of the space charge. Details of orthogonal mesh generation for multiply connected regions are given in Thompson *et al.* [28]. In that paper the functions $\varphi(x, y)$ and $\psi(x, y)$ again represent the coordinate lines of the mesh but the functions $a(\psi)$ and $\sigma(\varphi, \psi)$ described in this paper are replaced by more general user defined functions which allow control over the mesh spacing throughout the domain. The solution of the space charge problem can thus be viewed (almost) as a subset of the set of problems related to mesh generation. However, it is evident from this paper that the particular structure of the space-charge problem, and in particular the description of the function $\sigma(\varphi, \psi)$ by the simple ordinary differential equation (3.4b) allows us to use a rapidly convergent algorithm to generate an orthogonal mesh. To illustrate this we present in Figs. 13a and b two orthogonal body-fitted meshes generated by the space charge algorithm described in Budd and Wheeler [6] for simply or one connected domain for a configuration comprising the nose cone of an aircraft placed inside a cylindrical container. Both calculations took about 1 min cpu time on a VAX 11/780. Although our algorithm does not allow quite the same freedom in prescribing the mesh as Thompson's technique we do have two easily varied factors at our disposal. Namely, the distribution of the field lines on the nose cone of the aircraft (which is assumed to be the conductor

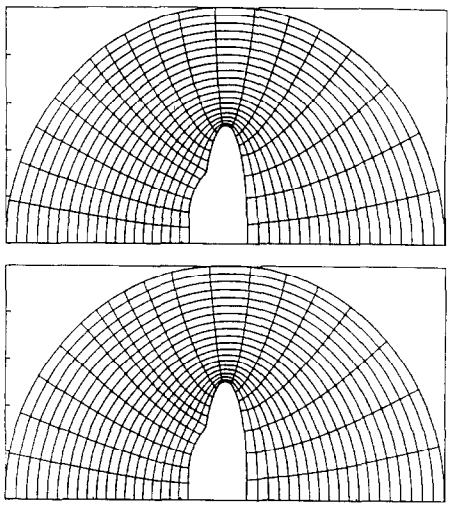

FIG. 13. Orthogonal grid using the space charge algorithm for the case of an aircraft nose cone in a cylindrical domain using two different space charge distributions on the nose cone.

at a high potential) and also the distribution of the space charge there. In general, the higher the space charge the wider apart will be the resulting field lines due to the mutual repulsion of the space charge flowing along these lines. Thus our algorithm appears to be both an effective means of solving the space charge problem and of generating meshes on which quite different problems may be solved.

ACKNOWLEDGMENT

One of us, C.J.B. gratefully acknowledges the financial support of the Central Electicity Generating Board, U.K.

REFERENCES

1. M. ABDEL-SALAM, M. FARGHALY, AND S. ABDEL-SATTAR, *IEEE Trans. Power Appar. Syst.* **PAS-101**, 4079 (1982).
2. M. ABDEL-SALAM, M. FARGHALY, AND S. ABDEL-SATTAR, *IEEE Trans. Electr. Insul.* **EI-18**, 110 (1983.
3. R. ARINA, Thesis, Von Karman Institute, Brussels 1987 (unpublished).
4. P. ATTEN, *C.R. Acad. Sci. Paris* **266**, 1188 (1968).
5. C. J. BUDD, A. FRIEDMAN, J. MCLEOD, AND A. A. WHEELER, *SIAM J. Appl. Math.* **50**, 181 (1990).
6. C. J. BUDD AND A. A. WHEELER, *Proc. R. Soc. London A* **417**, 389 (1988).
7. C. J. BUDD, *Eur. J. Appl. Math.* **2**, 43 (1991).
8. T. CHAN AND D. RESASCO, *SIAM J. Num. Anal.* **23**, 913 (1986).
9. R. CORBIN, CEGB Report TPRD/L/ES0680/M87, 1987 (unpublished).
10. R. COURANT AND D. HILBERT, *Methods of Mathematical Physics* (Springer-Verlag, Berlin, 1939).

11. J. Cross, *Electrostatics, Principals, Problems and Applications* (Adam Hilger, Bristol, 1987).
12. I. Duff, A. Erisman, and J. Reid, *Direct Methods for Sparse Matrices* (Clarendon Press, Oxford, 1986).
13. P. Esclangon and J. Planchard, *Electricité de France*, HI/4954-07, 1984 (unpublished).
14. N. Felici, *Direct Curr.* 252 (1963).
15. A. Hutton, CEGB Report TPRD/B/0868/P86, 1986 (unpublished).
16. D. Jacobs, CERL Report RD/L/N66/72, 1972 (unpublished).
17. W. Janischewskyj and G. Gela, *IEEE Trans. Power Appar. Syst.* **PAS-98**, 1000 (1979).
18. N. Kaptzow, *Elektrische vorgange in Gasen und im Vacuum* (Springer-Verlag, Berlin, 1955).
19. M. Khalifa, *IEEE Trans. Power Appar. Syst.* **PAS-87**, 1648 (1968).
20. Mesakian, private communication (1988).
21. R. Morrow, *Phys. Rev. A* **32**, 1799 (1985).
22. H. Okubo, M. Ikeda, M. Honda, and T. Yanari, *IEEE Power Appar. Syst.* **PAS-101**, No. 10, 4039 (1982).
23. M. Sarma and W. Janischewkyj, *IEEE Power Appar. Syst.* **PAS-88**, 718 (1969).
24. R. Sigmond, in *Electical Breakdown of Gases*, edited by M. Meek and J. D. Craggs (Wiley, New York, 1978), p. 319.
25. G. D. Smith, Numerical solution of partial differential equations: Finite difference methods (Oxford Univ. Press, London, 1985).
26. S. Smith, *IMA JAM* **39**, 189 (1987).
27. Y. Sunaga and Y. Sawada, *IEEE Power Appar. Syst.* **PAS-99**, 605 (1980).
28. J. Thompson, F. Thames, and C. W. Mastin, *J. Comput. Phys.* **24**, 1977 (1977).
29. J. S. Townsend, *Philos. Mag. J. Sci., Ser. 6* **28**, 83 (1914).
30. L. N. Trefethen, *SIAM J. Sci. Statist. Comput.* **1**, 82 (1980).
31. E. Varley, Oxford Study Group Report, 1985 (unpublished).